Fe2O3 Nanoparticle Seed Catalysts Enhance Cyclability on Deep (Dis)charge in Aprotic Li-O2 Batteries

Li, Zhaolong; Ganapathy, Swapna; Xu, Yaolin; Zhu, Quanyao; Chen, Wen; Kochetkov, Ivan; George, Chandra; Nazar, Linda F.; Wagemaker, Marnix

DOI
10.1002/aenm.201703513

Publication date
2018

Document Version
Final published version

Published in
Advanced Energy Materials

Citation (APA)
Li, Z., Ganapathy, S., Xu, Y., Zhu, Q., Chen, W., Kochetkov, I., George, C., Nazar, L. F., & Wagemaker, M. (2018). Fe2O3 Nanoparticle Seed Catalysts Enhance Cyclability on Deep (Dis)charge in Aprotic Li-O2 Batteries. *Advanced Energy Materials*, (1703513), 1-9. https://doi.org/10.1002/aenm.201703513

Fe_2O_3 Nanoparticle Seed Catalysts Enhance Cyclability on Deep (Dis)charge in Aprotic Li—O_2 Batteries

*Zhaolong Li, Swapna Ganapathy, Yaolin Xu, Quanyao Zhu, Wen Chen, Ivan Kochetkov, Chandramohan George, Linda F. Nazar, and Marnix Wagemaker**

Although the high energy density of Li—O_2 chemistry is promising for vehicle electrification, the poor stability and parasitic reactions associated with carbon-based cathodes and the insulating nature of discharge products limit their rechargeability and energy density. In this study, a cathode material consisting of α-Fe_2O_3 nanoseeds and carbon nanotubes (CNT) is presented, which achieves excellent cycling stability on deep (dis)charge with high capacity. The initial capacity of Fe_2O_3/CNT electrode reaches 805 mA h g^{-1} (0.7 mA h cm^{-2}) at 0.2 mA cm^{-2}, while maintaining a capacity of 1098 mA h g^{-1} (0.95 mA h cm^{-2}) after 50 cycles. The operando structural, spectroscopic, and morphological analysis on the evolution of Li_2O_2 indicates preferential Li_2O_2 growth on the Fe_2O_3. The similar d-spacing of the (100) Li_2O_2 and (104) Fe_2O_3 planes suggest that the latter epitaxially induces Li_2O_2 nucleation. This results in larger Li_2O_2 primary crystallites and smaller secondary particles compared to that deposited on CNT, which enhances the reversibility of the Li_2O_2 formation and leads to more stable interfaces within the electrode. The mechanistic insights into dual-functional materials that act both as stable host substrates and promote redox reactions in Li—O_2 batteries represent new opportunities for optimizing the discharge product morphology, leading to high cycling stability and coulombic efficiency.

1. Introduction

Rechargeable aprotic Li–air or Li—O_2 batteries have great potential to enable energy-hungry applications, owing to their extremely high theoretical specific energy density.[1–4] In typical aprotic Li—O_2 batteries, the (dis)charge process proceeds via the formation (oxygen reduction reaction, ORR) and decomposition (oxygen evolution reaction, OER) of Li_2O_2 according to the reaction $2Li + O_2 \underset{\text{charge}}{\overset{\text{discharge}}{\rightleftharpoons}} Li_2O_2$.[1] Therefore, the performance of this battery is determined by the reversibility of Li_2O_2 redox and the electrolyte stability.[1] The morphology and mechanism of Li_2O_2 deposition depends on the relative stability of the intermediate LiO_2 product in the electrolyte and the time scale of the Li_2O_2 formation on the cathode surface. While LiO_2 stability is determined by the stabilization of the Li^+ both through the solvation strength of the electrolyte (quantified by the donor number (DN)) and the association strength of the counter anion,[5–7] the time scale determines to what extent the intermediate LiO_2 species are solvated.[8] In an intermediate DN electrolyte, such as tetraethylene glycol dimethyl ether (TEGDME), the nucleation and growth of toroidal Li_2O_2 particles were proposed to occur via the solution dismutase mechanism at low current rates, whereas at fast rates quasi-amorphous thin films were observed on electrode surface.[8] Porous carbon based materials have been extensively explored as O_2 gas diffusion electrodes because of their high surface area, low weight, and low cost. Unfortunately, the discharge product Li_2O_2 reacts with carbon and the electrolyte at high potentials that characterize the OER process, and forms byproducts that clog the electrode pores, resulting in capacity fading and poor cycling stability.[9,10] Significant efforts have been expended in mitigating these side reactions by employing several combinations of noble metals (Au, Ru/RuO_2, and Pt),[11–21] transition metal oxides (MnO_2, Co/CoO/Co_3O_4, NiO, and TiO_2),[22–33] and metal-related compounds,[34–40] both as catalysts and conductive matrices to improve the energy efficiency and cycle life of the Li—O_2 batteries.

Most often the reported cycling performance of Li—O_2 systems is based on capacity-limited cycling, rather than the preferred potential-limited cycling where the full electrode capacity is utilized. Capacity-limited cycling performance of batteries makes it difficult to quantify if improved cycling stability can be attributed to the specific role of electrode or to the continuous consumption of new active sites on the electrode surface is delivered. To date, the only electrode systems that have displayed improved reversible Li_2O_2 formation and decomposition during potential limited cycling in aprotic Li—O_2 batteries are porous gold,[14] metallic RuO_2,[41,42] the metallic porous

Z. Li, Dr. S. Ganapathy, Y. Xu, Dr. C. George, Prof. M. Wagemaker
Department of Radiation Science and Technology
Delft University of Technology
Mekelweg 15, 2629JB Delft, The Netherlands
E-mail: m.wagemaker@tudelft.nl

Prof. Q. Zhu, Prof. W. Chen
State Key Laboratory of Advanced Technology for Materials Synthesis and Processing
School of Materials Science and Engineering
Wuhan University of Technology
Wuhan 430070, P. R. China

I. Kochetkov, Prof. L. F. Nazar
Department of Chemistry and the Waterloo Institute for Nanotechnology
University of Waterloo
Waterloo, Ontario N2L 3G1, Canada

The ORCID identification number(s) for the author(s) of this article can be found under https://doi.org/10.1002/aenm.201703513.

DOI: 10.1002/aenm.201703513

Magnéli phase Ti_4O_7,[43] and TiC.[37] However, Ru and Au are heavy elements that limit their gravimetric energy density, and their high cost makes them unlikely candidates for practical Li—O_2 batteries. TiC-based cathodes also exhibit good capacity retention but have a relatively low gravimetric capacity (about 350 mA h g^{-1} in dimethyl sulfoxide (DMSO) electrolyte and 520 mA h g^{-1} in TEGDME electrolyte),[37] and the same holds true for Ti_4O_7 electrodes.[43] Alternatively, iron and iron oxide are both low-cost and abundant, and carbon-supported iron-based catalysts[44–47] have been studied as O_2 diffusion electrodes for Li—O_2 batteries. Although iron oxide electrodes have been shown to exhibit lower overpotential, a higher capacity and better cycling performance compared to carbon electrodes upon capacity-limited cycling, full (dis)charge (with potential limited cycling) has not been reported to date, which is in fact a key figure-of-merit for these batteries.

Hematite Fe_2O_3 is known as a O_2 reduction catalyst in aqueous media[48,49] and as an O_2 adsorption material.[50] While it is ostensibly a wide band gap semiconductor, the presence of structrual defects leads to significant electronic conductivity.[50] Shimizu et al.[48] and Sun et al.[49] found that via its catalytic activity, Fe_2O_3 could alter the ORR reaction pathway from a $2e^-$ to a $4e^-$ process in aqueous media. Gurlo et al.[50] have reported that oxygen could preferentially absorbs on the α-Fe_2O_3 surface, and Zhang et al.[33] found that Co_3O_4 acted as crystal seed by preferential oxygen adsorption, facilitating the formation of Li_2O_2 film and particles. Motivated by these observations, our work reported here demonstrates that oxygen cathodes prepared by a combination of nanosized Fe_2O_3 seed crystallites with carbon nanotubes (CNT) exhibit an impressive cycle stability and large capacity when cycled in a large potential cutoff window of 2.0–4.5 V. The initial specific capacity of the Fe_2O_3/CNT electrode reaches about 805 mA h g^{-1} (0.70 mA h cm^{-2}), and it maintains a reversible capacity of ≈1098 mA h g^{-1} (0.95 mA h cm^{-2}) after 50 cycles at a current density of 0.2 mA cm^{-2}. We propose that the similar (104) Fe_2O_3 and (100) Li_2O_2 lattice plane d-spacing induces epitaxial growth of Li_2O_2 on the Fe_2O_3 surface. The epitaxial growth enhances the nucleation of Li_2O_2 which enhances its crystallinity, and suppresses amorphous Li_2O_2 formation which leads to passivation. This epitaxial growth of Li_2O_2 on Fe_2O_3 nanoparticles results in oriented and smaller secondary Li_2O_2 particles, which are responsible for more facile decomposition upon oxidation. The preferential formation of Li_2O_2 on Fe_2O_3 and the facile decomposition are proposed to be responsible for the significantly improved reversible Li_2O_2 formation and decomposition leading to the observed high capacity retention on deep (dis)charge.

2. Results and discussion

2.1. Electrochemical Performance

The use of Fe_2O_3 nanoseed crystals in the gas diffusion cathode was also motivated by our previous study, where hexagonal NiO nanocrystals ($a = b = 2.972 \pm 0.001$ Å, $c = 7.158 \pm 0.001$ Å) were found to induce equiaxal growth of Li_2O_2 ($a = b = 3.142 \pm 0.005$ Å, $c = 7.650 \pm 0.005$ Å) due to an approximate match of their a- and b-lattice parameters.[30] The lattice parameters of the α-Fe_2O_3 ($a = b = 5.5035$ Å and $c = 13.74$ Å) are distinct from Li_2O_2; however, the interplanar spacing of its (104) (2.70 Å) and (110) (2.52 Å) planes are approximately equal to the (100) (2.72 Å) and (101) (2.56 Å) planes of Li_2O_2 (Figure S1, Supporting Information). The CNTs plays an important role in forming an interpenetrating porous network structure that facilitates access of O_2, and they also provide electronic conductivity across electrodes and support the Fe_2O_3 catalyst.

Figure 1 displays the galvanostatic (dis)charge cycle performance of Li—O_2 batteries with CNT and Fe_2O_3/CNT cathodes by employing a potential cutoff at different (dis)charge current densities. The Brunauer-Emmett-Teller (BET) surface of the cast Fe_2O_3/CNT cathodes (75/25 wt%) is smaller, 8.47 m^2 g^{-1}, compared to that of the CNT powder (150–200 m^2 g^{-1}). Therefore, the effective electrochemical surface area of Fe_2O_3/CNT electrodes must be significantly smaller compared to the CNT cathodes. This implies that when applying the same current density, based on the geometrical surface of the cathodes, the local current density should be expected to be larger for the Fe_2O_3/CNT cathodes. The cycling stability of the CNT cathode is relatively poor (Figure 1a–c), and after 30 cycles the specific discharge capacity decreases drastically at current densities of 0.1 and 0.2 mA h cm^{-2}. Under the same cycling conditions, despite the fact that the local current density should be larger, the Fe_2O_3/CNT cathode shows significantly better cycling stability and coulombic efficiency, as shown in Figure 1d–f. The reversible specific capacity on deep (dis)charge of the Fe_2O_3/CNT electrode reaches 1295 mA h g^{-1} after 50 cycles at a current density of 0.1 mA cm^{-2} (based on the total mass of the Fe_2O_3 and CNT), which is larger than the first discharge capacity (951 mA h g^{-1}). Also at a current density of 0.2 mA cm^{-2}, the initial specific discharge capacity of the Fe_2O_3/CNT cathode is 805 mA h g^{-1}, and it maintains a capacity of 1098 mA h g^{-1} after 50 cycles. The incremental capacity over cycling is most likely the result of continuous activation of the Fe_2O_3 surface due to the gradual impregnation of the electrolyte into the porous structure of CNT and Fe_2O_3 nanoparticles, which activates more reaction surface over time.[41]

Interestingly, after the first cycle the specific capacity of the Fe_2O_3/CNT cathode (normalized using geometric surface of the electrode) is larger than that of the CNT cathode (Figure S2, Supporting Information). Again we note that the electrochemical surface area of the Fe_2O_3 electrodes is expected to be smaller based on the smaller Fe_2O_3 surface area compared to that of CNT. The initial discharge capacity of the Fe_2O_3/CNT cathode is 0.6 and 0.7 mA h cm^{-2}, and 0.95 and 1.05 mA h cm^{-2} for the CNT cathode at current densities of 0.1 and 0.2 mA cm^{-2}, respectively (Figure S2, Supporting Information). However, after 30 deep (dis)charge cycles, the capacities of the CNT electrode dramatically drop to almost zero. On the contrary, the capacity of the Fe_2O_3/CNT electrode increases to 0.85 and 0.95 mA h cm^{-2} after 50 deep (dis)charge cycles at current densities of 0.1 and 0.2 mA cm^{-2}, respectively. The results indicate that the Fe_2O_3/CNT cathode surface is more active toward ORR compared to the CNT cathode, hence triggering the formation of more Li_2O_2. The charge overpotential of the Fe_2O_3/CNT electrode is 200 mV lower than that of the CNT cathode (Figure S3, Supporting Information), which was also observed in other studies.[44,45]

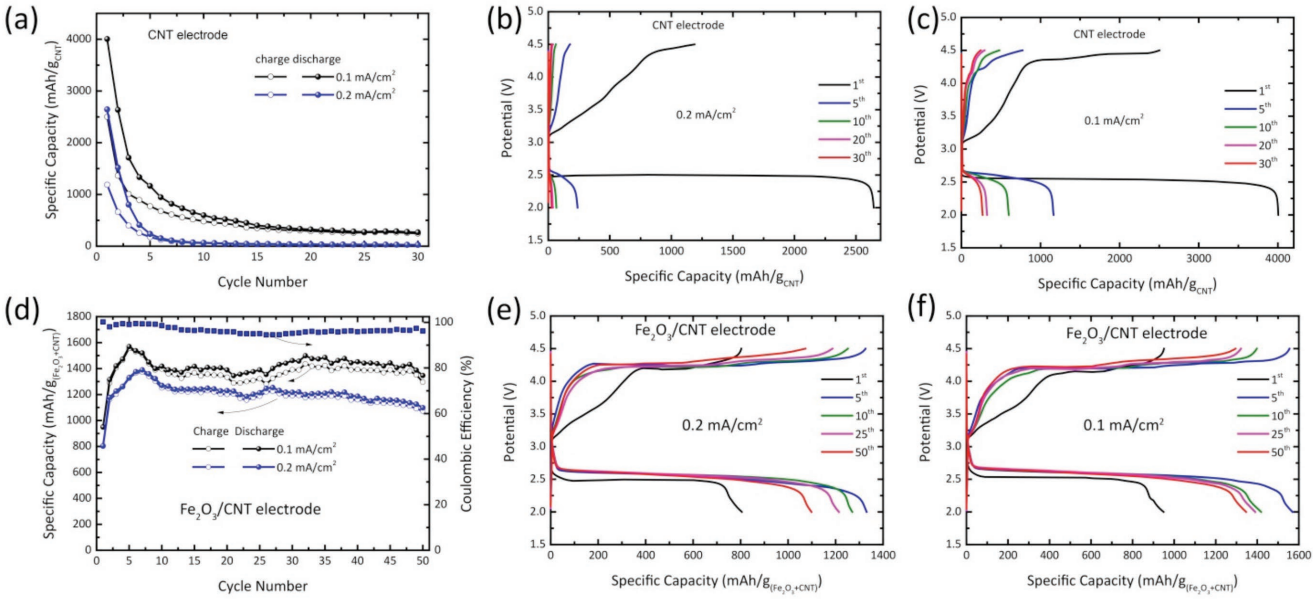

Figure 1. Cycling performance of a) CNT and d) Fe_2O_3/CNT oxygen cathodes during deep (dis)charge by employing a potential window of 2.0–4.5 V, measured in 0.5 M LiTFSI/TEGDME electrolyte at current densities of 0.1 and 0.2 mA cm^{-2}, respectively in Li—O_2 batteries at 1.0 bar O_2 pressure. b,c,e,f) selected, potential cutoff, galvanostatic (dis)charge profiles for CNT and Fe_2O_3/CNT oxygen cathodes, respectively.

As an anode in lithium-ion batteries, Fe_2O_3 nanostructured materials follow a series of Li-insertion processes resulting in two voltage plateaus at ≈1.2 and 0.75 V, respectively.[51,52] A Fe_2O_3/CNT electrode cycled in Ar within a 2.0–4.5 V window (Figure S4, Supporting Information) shows a reversible capacity of only 24 mA h g^{-1} (0.027 mA h cm^{-2}) at a current density of 0.1 mA cm^{-2}. On the other hand, in the presence of O_2, the Fe_2O_3/CNT cathode displays a stable discharge plateau at around 2.6 V, as shown in Figure 1e,f. Thus, within the potential window of 2.0–4.0 V, the Li-intercalation reaction does not contribute to the discharge capacity of the Fe_2O_3/CNT cathode in a Li—O_2 battery.

Figure S5 (Supporting Information) shows the cyclic voltammetry curves of CNT and Fe_2O_3/CNT cathodes, respectively. The observed bell shaped oxygen reduction curves of both the CNT and Fe_2O_3/CNT cathodes represent the expected formation of Li_2O_2.[53] Due to the low electronic conductivity of lithium oxide, the oxidation overpotential is expected to be high. The oxygen evolution anodic peaks can be attributed to the oxidation of Li_2O_2.[53,54]

2.2. Analysis of the Evolution of Products During (Dis)charge

In principle, the potential of a Li—O_2 battery system should sharply increase when the discharge product is completely decomposed during charge. This is typically observed in Li-ion battery electrodes, where after all of the removable lithium ions are extracted, the potential steeply increases toward the cutoff voltage. However, this phenomenon is seldom reported for Li—O_2 batteries, where capacity restriction is typically used to demonstrate the electrochemical performance of oxygen cathodes. Thereby, side reactions with the electrolyte that occur at large and small potentials are avoided, at the same time the reversibility is artificially improved as the battery is only partially discharged. Potential limited cycling utilizes the full capacity, and is more challenging, because side reactions are unavoidable in an aprotic Li—O_2 battery at high charge potentials. These parasitic reactions lead to the formation of Li_2CO_3, the decomposition of the electrolyte, and the decomposition of the binder in the cathode.[55]

To investigate the reversibility of the products on the Fe_2O_3/CNT oxygen cathodes at high charge potentials, the discharge capacity was restricted to 0.5 and 0.25 mA h and the Li—O_2 batteries were subsequently charged to 4.5 V at current densities of 0.1 and 0.2 mA cm^{-2}, respectively, as shown in Figure S6 (Supporting Information). Under these conditions the Li—O_2 battery also exhibits stable cycling, where the potential limited charge capacity is very close to the discharge capacity over 50 cycles (Figure S6a,d)). The discharge plateau is close to 2.6 V (Figure S6b–f). Notably, the charge voltage increases to 4.5 V at the end of the charge process following the stable charge plateaus, which is rarely reported for Li—O_2 battery (dis)charge profiles. From the ex situ X-ray powder diffraction (XRD) patterns shown in Figure S7a (Supporting Information), it is difficult to observe differences between the diffraction peaks of the pristine and discharged Fe_2O_3/CNT cathode at the current densities of 0.1 and 0.2 mA cm^{-2}, as expected owing to the similar lattice spacing of (104) Fe_2O_3 and (100) Li_2O_2 planes (Figure S1, Supporting Information). The scanning electron microscopy (SEM) images also show no significant difference between the pristine sample (Figure S7b, Supporting Information) and the discharged cathode (Figure S7c, Supporting Information), with the exception of a film-like structure that forms at a current density of 0.2 mA cm^{-2}. This most likely represents the deposition of a quasi-amorphous thin Li_2O_2 film, which is known to occur at high (dis)charge currents.[8] Using the titration experiment developed by McCloskey and co-workers[56] (Figure S8,

Supporting Information), the yield of Li_2O_2 after first discharge to 2.0 V on the surface of Fe_2O_3/CNT cathodes was found to be 95.7% and 96.5% compared to the theoretical capacity at the current density of 0.2 and 0.1 mA cm^{-2}, respectively, confirming that the discharge capacity from the Fe_2O_3/CNT cathode is mainly due to the formation of Li_2O_2. Online electrochemical mass spectrometry (OEMS) measurements were performed to quantify the O_2 evolution during charge (Figure S9, Supporting Information). Even though O_2 evolution does not match the number of electrons involved in the first charge in the OEMS experiment, only O_2 is detected over the charge plateau (Figure S9a, Supporting Information). At the end of charge, CO_2 is generated from the decomposition of some carbonates that are unavoidably generated via reaction of superoxide and/or peroxide with the electrolyte. This is the reason for the lower e^-/O_2 ratio in Figure S9b (Supporting Information) (compared to the theoretical value of $2e^-/O_2$ corresponding to pure O_2 evolution); namely, some byproducts form that are not related to the evolution of O_2. Unfortunately, despite the increased columbic efficiency, the stability of all the cell components (electrolyte, CNT conductive support, etc.) in the electrolyte with an intermediate donor number still needs to be addressed in order to obtain a ratio of 2.0 e^-/O_2. However, the aim of this study is to show the beneficial impact of the Fe_2O_3 on the reversible growth of Li_2O_2, resulting in the improved cycling under potential limited cycling.

To verify the formation and decomposition of Li_2O_2 on the Fe_2O_3/CNT cathode, operando XRD was carried out on a Li—O_2 battery cycled within a potential window of 2.0–4.5 V at a current density of 0.2 mA cm^{-2} in a 0.5 M LiTFSI/TEGDME electrolyte (**Figure 2**). Since the (104) and (110) lattice plane distances of Fe_2O_3 are very similar to the (100) and (101) planes of Li_2O_2, respectively (Figure S1, Supporting Information), the reflections are indistinguishable in ex situ XRD measurements of discharged cathodes, especially due to the broadening of nanosized Fe_2O_3 peaks. However, the 2D contour operando XRD patterns in the 2θ region of 31.5–37° (Figure 2) show a symmetric broadening of the (100)/(104) and the (101)/(110) Li_2O_2/Fe_2O_3 lattice planes, confirming the gradual formation and decomposition of Li_2O_2.

To further investigate the discharge product formed on the cathode surface at a current density of 0.2 mA cm^{-2}, ex situ X-ray photoelectron spectroscopy (XPS) analysis (**Figure 3**) was carried out on the pristine Fe_2O_3/CNT cathode and cathodes from discharged and recharged batteries (discharge to 2.0 V and recharge to 4.5 V; the electrochemical performance of these batteries is shown in Figure S10 in the Supporting Information). All spectra were calibrated using the C1s peak of CNT at 284.48 eV. The survey scan from 0 to 800 eV is given in Figure 3a and shows the relative change in the quantities of oxygen, lithium, and iron on the surface of the Fe_2O_3/CNT cathodes. The relative intensity of the Fe2p peaks for the Fe_2O_3/CNT cathodes diminishes after the first and fifth discharge (black and blue lines in Figure 3a), but recovers after recharge (red line in Figure 3a), indicating that the surface of the cathode is covered with a discharge product which is removed after charge. Figure 3b–d displays the XPS spectra in the Fe2p, O1s, and Li1s/Fe3p regions, respectively. The Fe2p region from 705 to 730 eV shows the characteristic $2p_{1/2}$ and $2p_{3/2}$ doublet which is attributed to Fe_2O_3 (pink line in Figure 3b).[57] After the first discharge, the peak becomes less prominent (black line in Figure 3b), and after the fifth discharge the peak becomes indistinguishable (blue line in Figure 3b). However, when the cathode is recharged to 4.5 V, the Fe2p signal completely reappears, and is similar to the pristine sample (red and pink lines in Figure 3b). This is an indication of the formation and decomposition of products on the cathode surface during (dis)charge. In addition, after first discharge, the main peak of Fe2p slightly shifts to low binding energy compared to the pristine and recharged cathodes, which may be attributed to the surface redox activities (involving $Fe^{2+/3+}$ redox couple). Further, this could probably overlap with the surface bonds between Li_2O_2 and Fe_2O_3. In the pristine electrode, O1s spectral peaks (pink line in Figure 3c) appear from 528 to 533 eV and can be assigned to Fe—O and Fe—OH from Fe_2O_3.[57] The features (pink line in Figure 3d) in the region from 55.5 to 57.3 eV can be attributed to the Fe3p contribution from Fe_2O_3. It is interesting to note that after the first and fifth discharge to 2.0 V, the spectral peaks in the O1s and Fe3p/Li1s regions (black and blue lines in Figure 3c,d) shift to binding energies of 54.6 and 531.2 eV, mainly corresponding to the lithium and oxygen contributions from

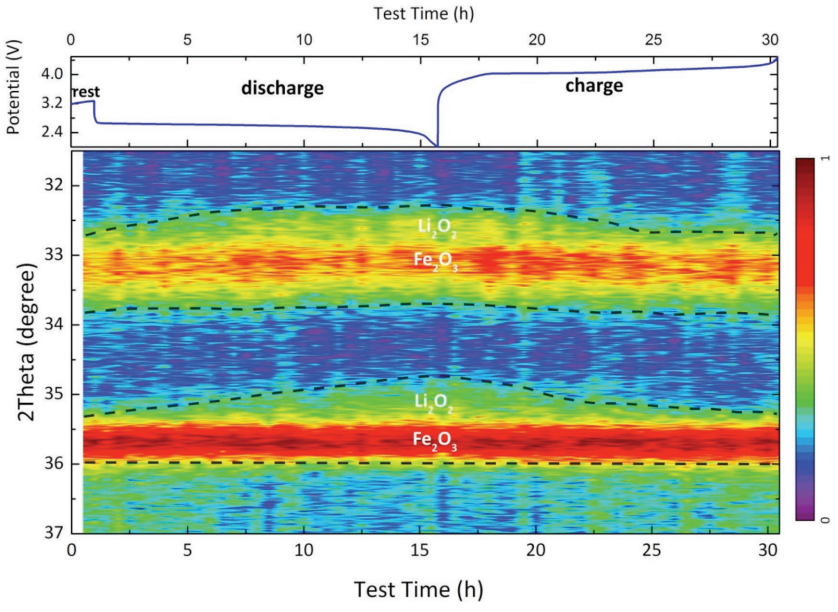

Figure 2. Top: (Dis)charge profile of the Fe_2O_3/CNT oxygen cathode in an operando Li—O_2 battery. Bottom: 2D contour plots of the operando XRD patterns showing the 2θ region between 31.5–37° during a complete (dis)charge cycle, demonstrating the formation of Li_2O_2 and its decomposition. The battery was (dis)charged using a 0.5 M LiTFSI/TEGDME electrolyte within a potential window of 2.0–4.5 V at a current density of 0.2 mA cm^{-2}.

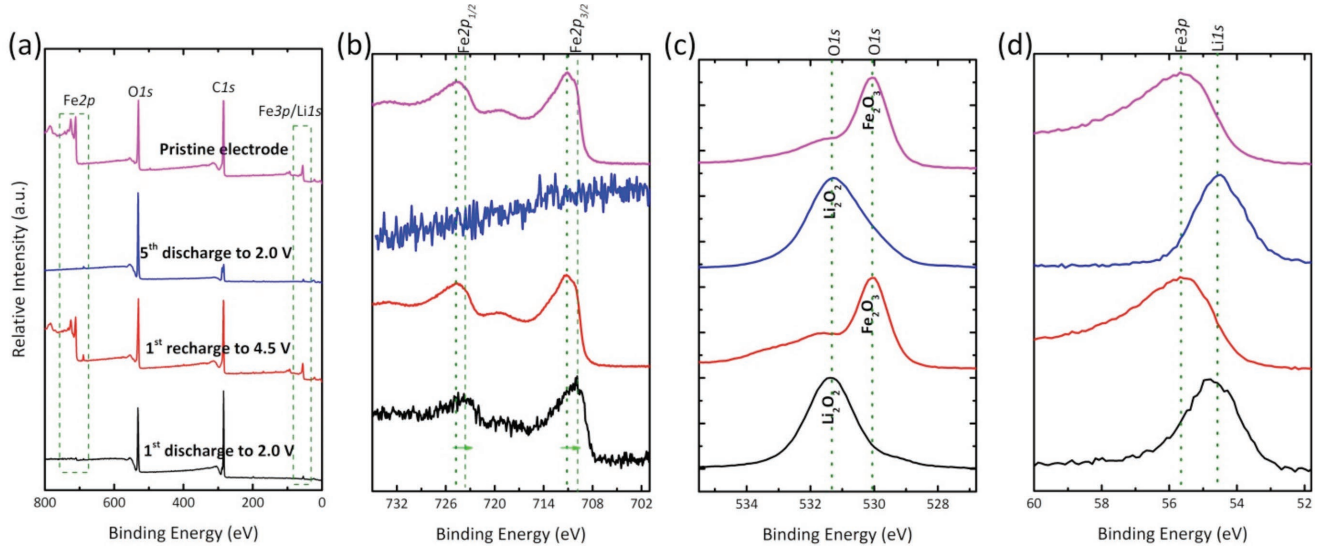

Figure 3. a) XPS survey scans of Fe_2O_3/CNT oxygen cathodes at different (dis)charge states. b,c,d) High resolution XPS in the Fe2p, O1s, and Li1s or Fe3p regions, respectively for the Fe_2O_3/CNT oxygen cathode at different states of (dis)charge. The black, red, blue, and pink lines represent the cathode at the state of first discharge to 2.0 V, first recharge to 4.5 V, fifth discharge to 2.0 V, and pristine states, respectively.

Li_2O_2, respectively.[58] Furthermore, after recharge (red line in Figure 3c,d), the shift of peaks in this region returns to their original positions, indicating reappearance of the Fe2p and Fe3p contributions and hence the removal of Li_2O_2 from the cathode surface. In summary, from the XPS analysis of the pristine, discharged and recharged samples, we conclude that Li_2O_2 is the main product formed reversibly on the Fe_2O_3/CNT cathode surface during (dis)charge in the Li—O_2 battery.

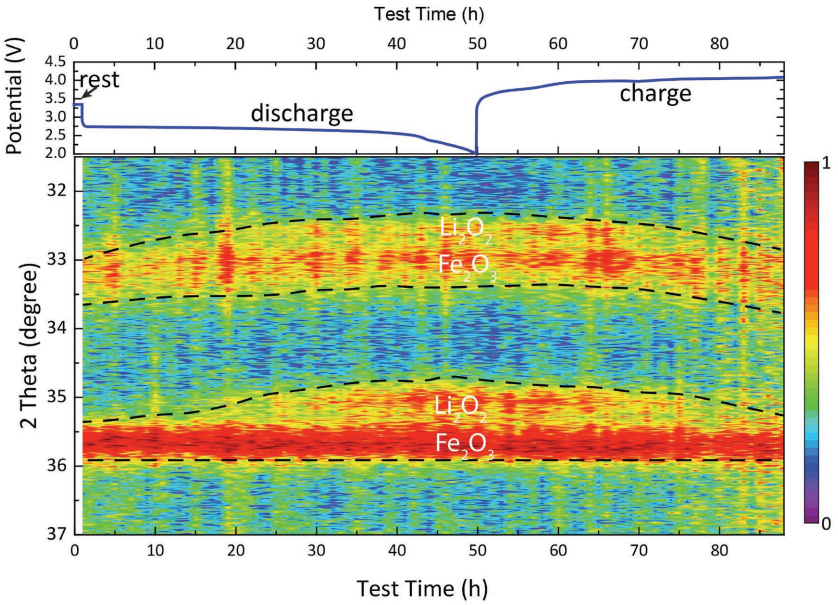

Figure 4. Top: (Dis)charge profile of the electrochemical performance of the Fe_2O_3/CNT oxygen cathode in an operando Li—O_2 battery. Bottom: 2D contour plots of the operando XRD patterns showing the 2θ region between 31.5–37°, during a complete (dis)charge cycle demonstrating the formation and decomposition of Li_2O_2. The operando Li—O_2 battery was (dis)charged using a 0.5 M LiTFSI/TEGDME electrolyte within a potential window of 2.0–4.5 V at a current density of 0.05 mA cm^{-2}.

Figure 4 shows the 2D contour plot of the operando XRD patterns of the Fe_2O_3/CNT cathode at a lower current density of 0.05 mA cm^{-2} compared to that shown in Figure 2. Discernable Li_2O_2 XRD peaks are observed on the Fe_2O_3/CNT cathode when the discharge current density is lowered to 0.05 mA cm^{-2} (**Figure 5**a). The gradual increase and decrease in the intensities of the Li_2O_2 reflections, corresponding to the (100) and (101) planes of Li_2O_2 (Figure 4), indicate the gradual formation and decomposition of Li_2O_2 on the Fe_2O_3/CNT cathode as a function of (dis)charge time. The ex situ SEM image of the Fe_2O_3/CNT cathode after discharge to 2.0 V shows a homogenous platelet morphology of the Li_2O_2 particles (Figure 5b). Based on the Rietveld refinement of the sequential operando XRD patterns (Figure 5c), we obtained the average coherent size of Li_2O_2 as a function of (dis)charge time (Figure 5d). During the refinement, the Fe_2O_3 parameters were fixed based on the refinement result as shown in Figure S11 (Supporting Information). The average coherent length of the Li_2O_2 crystallite platelets first increases during initial discharge, after which it decreases as discharge progresses. This indicates the formation of larger and more anisotropic shaped Li_2O_2 crystallites at the initial stages of discharge. The deposition of smaller and more isotropic Li_2O_2 occurs as discharge progresses, similar to what we reported previously.[59] During charge, smaller Li_2O_2 crystallites preferentially decompose followed by the decomposition of the larger Li_2O_2 crystallites, as can be concluded from the initial increase in the average coherence length of Li_2O_2 (after which it remains constant to the end of charge).[60]

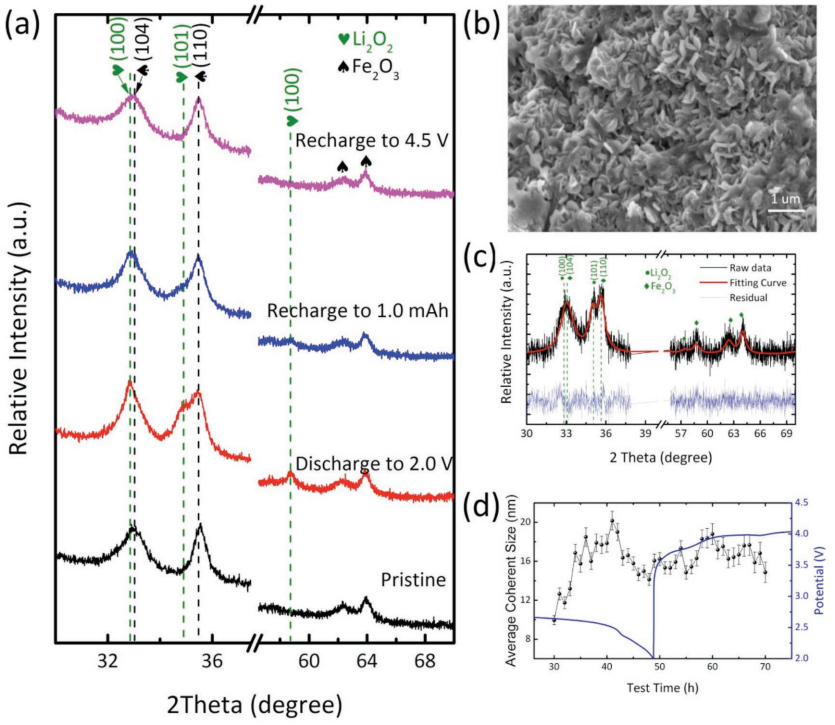

Figure 5. a) Ex situ XRD patterns of the Fe_2O_3/CNT cathode at different discharge and recharge states. b) SEM image of the Li_2O_2 particles formed on the Fe_2O_3/CNT cathode at the end of discharge. c) Rietveld refinement result of the XRD patterns. d) Average coherent size of Li_2O_2 obtained from Rietveld refinement as a function of (dis)charge time. The corresponding voltage profile measured during (dis)charge is illustrated in the graph.

the discharge is covered by Li_2O_2 with significantly smaller disc-like particles—about 300 nm in diameter and several tens of nanometer in thickness, and some large flower-like plates, several micrometers in diameter and a hundred nanometers in thickness. Notably, the Li_2O_2 disc-like particles on the Fe_2O_3/CNT cathode appear to be oriented perpendicular to the Fe_2O_3 surface and are more frequently vertically aligned. The difference in Li_2O_2 morphology between the CNT and Fe_2O_3/CNT cathodes suggests a different growth mechanism induced by the Fe_2O_3 nanoparticles. In the presence of Fe_2O_3 nanoparticles, at low discharge current density, disc like rather than toroidal Li_2O_2 particles are formed, some of which grow into flower-like structures. The cycling performance of the Fe_2O_3/CNT cathode at a current density of 0.02 mA cm^{-2} upon deep (dis)charge is represented in Figure S12 (Supporting Information). The rather good cycling stability and high coulombic efficiency (exceeding 90%) over the first 20 cycles again suggest that the Li_2O_2 morphology on the Fe_2O_3/CNT cathode allows for more stable cycling compared to that on the CNT cathodes under comparable conditions.

Figure 6 displays XRD patterns and SEM images of the discharge product formed on the cathode surface at even lower current densities (0.02 mA cm^{-2}). Very evident Li_2O_2 peaks are observed in the XRD patterns of both the discharged CNT and Fe_2O_3/CNT cathodes, as shown in Figure 6a. After complete discharge at a current density of 0.02 mA cm^{-2}, the surface of the CNT cathode (Figure 6b,c) shows homogenous toroidal Li_2O_2 particles—about 500 nm in diameter and 100 nm in thickness, randomly oriented on the cathodes. In contrast, the surface of the Fe_2O_3/CNT cathode (Figure 6d,e) at the end of

3. Mechanism

Since TEGDME has an intermediate DN, Li_2O_2 formation is expected to take place both via formation in the solvent and directly on the surface of the cathode.[5,6] The different Li_2O_2 morphology obtained upon adding Fe_2O_3 to the CNT cathodes, observed in the SEM images in Figure 6b–e, demonstrates that the presence of Fe_2O_3 influences the growth mechanism of the Li_2O_2 particles. In this context, we remind that Fe_2O_3 is a wide band gap hopping semiconductor, but the presence of extensive

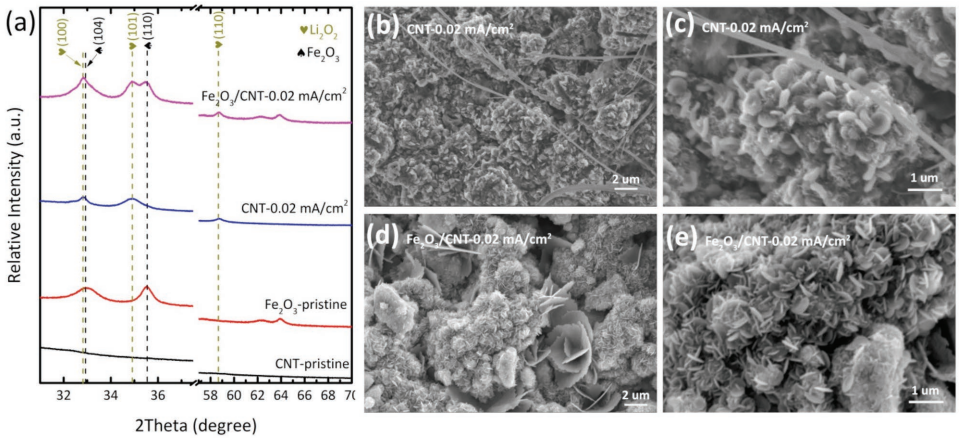

Figure 6. a) The Li_2O_2 and Fe_2O_3 XRD reflections resulting from CNT and Fe_2O_3/CNT oxygen cathodes at the end of complete discharge, respectively. b, c) and d, e) SEM images of the CNT cathode and the FeO_3/CNT cathode at the end of discharge at a current density of 0.02 mA cm^{-2}.

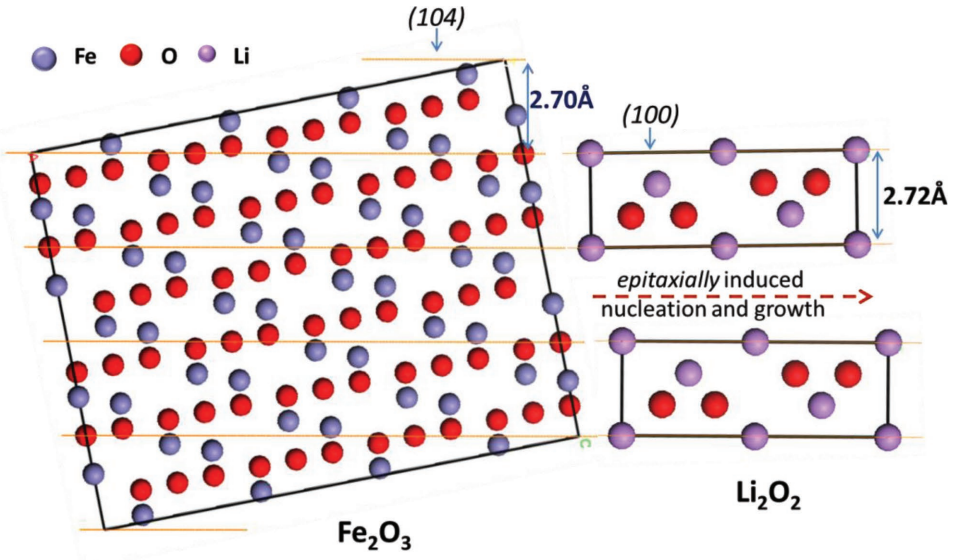

Figure 7. Schematic of the proposed "epitaxially induced nucleation and growth" mechanism of Li_2O_2 on Fe_2O_3. The Fe_2O_3 crystallites expose the (104) lattice spacing at their surface, which matches the (100) lattice distance of the Li_2O_2 crystallites, which grow in the (001) direction perpendicular to the Fe_2O_3 surface.

defects leads to significant electronic conductivity. Previously, hexagonal NiO nanoparticles were used as nanoseed crystals to induce equiaxal growth of Li_2O_2 owing to their similar *a*- and *b*-lattice parameters.[30] The Fe_2O_3 nanoseed particles have even more similar interplanar spacing to that of Li_2O_2, as shown in **Figure 7** and Figure S1 (Supporting Information). In the XRD pattern of the Fe_2O_3 nanoparticles, the (104) reflection is broader than the (110) reflection (Figure S11, Supporting Information), reflecting the anisotropic shape of the Fe_2O_3 nanoparticles.[58] High resolution transmission electron microscopy (HRTEM) image (Figure S14, Supporting Information) indicates that the Fe_2O_3 nanoparticles have a 2D shape, where the long-dimension is along the [hk0] direction and the short-dimension is along the [00l] direction. TEM image also shows that the interplanar spacing on the surface of the Fe_2O_3 crystallites is close to 0.27 nm. The similar value of the d-spacing of the Li_2O_2 (100) lattice planes (0.272 nm in Figure S1 in the Supporting Information) led us to hypothesize a "epitaxially induced nucleation and growth" mechanism for Li_2O_2 growth on Fe_2O_3. This mechanism is schematically shown in Figure 7 where (1) the Li_2O_2 crystallite nucleates on the [0k0] surface facets of the Fe_2O_3 crystallite; (2) because the dominant Li_2O_2 growth direction is (001),[60,61] and the footprint of the Li_2O_2 crystallite is in the (100)/(010) direction, which matches on the (104) lattice plane exposed on the Fe_2O_3 surface. This is consistent with the disc-like Li_2O_2 particles that appear to grow perpendicular to the Fe_2O_3/CNT electrode surface observed in Figure 6d,e. The Rietveld refinement shows no significant change in lattice parameters of the Li_2O_2 that forms on the CNT and F_2O_3/CNT cathodes (Figure S13 and Table S1, Supporting Information) in contrast to NiO.[30]

It is established that the current density affects the morphology of the Li_2O_2 formed.[8] This is also confirmed by the present XRD studies where the average coherent length of Li_2O_2 at relatively low current density (0.02 mA cm^{-2}) (Table S1, Supporting Information) is larger than that at high current density (0.05 mA cm^{-2}) (Figure 5d) on the Fe_2O_3/CNT electrode. Interestingly, comparing the XRD refinement results (Table S1, Supporting Information) of the average coherent length of Li_2O_2 crystallites, the larger and much more isotropic Li_2O_2 crystallites are formed on the Fe_2O_3/CNT cathodes compared to that on CNT cathode. However, comparing the SEM images in Figures 5b and 6b,e suggests that significantly smaller disc-like Li_2O_2 secondary particles form on Fe_2O_3/CNT cathodes. The smaller secondary particles will be easier to decompose upon charge due to their relatively higher surface area. Another aspect of the proposed epitaxial growth mechanism is that the larger crystallites indicate that the Fe_2O_3 enhances the crystallinity of the Li_2O_2, thus suppressing the formation of passivating amorphous films, as also observed on NiO seed crystallites,[30] and enhances reversiblity of Li_2O_2. This is particularly noteworthy as the local current density is most likely much larger on the Fe_2O_3/CNT cathodes because of their smaller surface area. Another advantage is that at high charge potentials the Li_2O_2–Fe_2O_3 interface can be expected to more stable than Li_2O_2–carbon interface, which forms a thin isolating Li_2CO_3 film.[10] In this context, it is important to note that hematite Fe_2O_3 nanostructures exhibit good electronic conductivity,[50,62,63] necessary for the electron transport between the carbon matrix and the Li_2O_2. Finally, preferential adsorption of oxygen onto the surface of α-Fe_2O_3 surface[64] may promote the deposition of Li_2O_2 on the Fe_2O_3 surface.

These favorable properties of α-Fe_2O_3 most likely contributing to the reversible growth of Li_2O_2 provide a rationale for the improved reversibility upon potential-limited cycling of the Fe_2O_3/CNT cathodes in direct comparison to the CNT cathodes. As discussed, the Fe_2O_3 impacts the reversible formation of Li_2O_2, which appears to be the origin of the improved reversibility; however, this is not expected to prevent detrimental reactions between the intermediate discharge products and the electrolyte. The relatively large coulombic

efficiency (≈ >95% for Li_2O_2 production), especially under potential limited cycling conditions, in combination with the titration results suggests a reduction in the degree of side reactions. Possibly, faster Li_2O_2 nucleation induced by Fe_2O_3 may reduce the exposure time of intermediate discharge products. However, the far from theoretical O_2 evolution measured by OEMS indicates that parasitic reactions as generally observed for this system or reversible reactions that do not involve O_2 evolution cannot be excluded, which will be topic for further investigations.

4. Conclusions

In conclusion, we have demonstrated that a Li—O_2 battery consisting of an Fe_2O_3/CNT oxygen cathode with TEGDME electrolyte offers more reversible cycling on deep potential-restricted (dis)charge with a capacity retention of ≈1098 mA h g^{-1} (0.95 mA h cm^{-2}) after 50 cycles at a current density of 0.2 mA cm^{-2}. Operando XRD and ex situ XPS measurements reveal the reversible formation and decomposition of Li_2O_2 crystallites during (dis)charge at high and intermediate current densities (0.2 and 0.05 mA cm^{-2}). At low current densities (0.02 mA cm^{-2}) small disc-like particles and some large plates of Li_2O_2 form perpendicular to the Fe_2O_3/CNT electrode surface, which are very different from that of toroidal Li_2O_2 particles formed on the CNT electrode. Based on the similar lattice spacing of the (104)/(100) reflections in Fe_2O_3/Li_2O_2, we have hypothesized a "epitaxially induced nucleation and growth" mechanism. The resulting Li_2O_2 has a more isotropic crystallite shape and a smaller secondary particle size, where the epitaxial growth and the larger surface area appear to be responsible for the improved reversibility of the Li_2O_2 formation and oxidation. Although electrolyte stability remains a critical issue, the "epitaxially induced nucleation and growth" mechanism proposed in this work can be potentially used to gain control over the Li_2O_2 growth and thereby improve the electrochemical performance of Li—O_2 batteries.

Supporting Information

Supporting Information is available from the Wiley Online Library or from the author.

Acknowledgements

The authors thank Kees Goubitz, Michel Steenvoorden, and Frans Ooms for their assistance with experiments. The authors greatly acknowledge financial support from the China Scholarship Council (CSC), the grants (National Natural Science Foundation of China (51472189)) from Q.Z. The research leading to these results has received funding from the European Research Council under the European Union's Seventh Framework Program (FP/2007-2013)/ERC Grant Agreement no. [307161] of M.W. L.N. gratefully acknowledges NSERC for financial support. FlexBatteries (grant agreement no.704659) from Marie Skłodowska-Curie action is also acknowledged.

Conflict of Interest

The authors declare no conflict of interest.

Keywords

aprotic Li—O_2 batteries, deep (dis)charge, epitaxial growth mechanism, Fe_2O_3 seed catalysts

Received: December 13, 2017
Revised: January 31, 2018
Published online:

[1] D. Aurbach, B. D. McCloskey, L. F. Nazar, P. G. Bruce, *Nat. Energy* **2016**, *1*, 16128.
[2] A. C. Luntz, B. D. McCloskey, *Chem. Rev.* **2014**, *114*, 11721.
[3] J. Lu, L. Li, J.-B. Park, Y.-K. Sun, F. Wu, K. Amine, *Chem. Rev.* **2014**, *114*, 5611.
[4] R. Black, B. Adams, L. F. Nazar, *Adv. Energy Mater.* **2012**, *2*, 801.
[5] L. Johnson, C. Li, Z. Liu, Y. Chen, S. A. Freunberger, P. C. Ashok, B. B. Praveen, K. Dholakia, J. M. Tarascon, P. G. Bruce, *Nat. Chem.* **2014**, *6*, 1091.
[6] N. B. Aetukuri, B. D. McCloskey, J. M. García, L. E. Krupp, V. Viswanathan, A. C. Luntz, *Nat. Chem.* **2015**, *7*, 50.
[7] C. M. Burke, V. Pande, A. Khetan, V. Viswanathan, B. D. McCloskey, *Proc. Natl. Acad. Sci. USA* **2015**, *112*, 9293.
[8] B. D. Adams, C. Radtke, R. Black, M. L. Trudeau, K. Zaghib, L. F. Nazar, *Energy Environ. Sci.* **2013**, *6*, 1772.
[9] B. D. McCloskey, R. Scheffler, A. Speidel, G. Girishkumar, A. C. Luntz, *J. Phys. Chem. C* **2012**, *116*, 23897.
[10] B. D. McCloskey, A. Speidel, R. Scheffler, D. C. Miller, V. Viswanathan, J. S. Hummelshøj, J. K. Nørskov, A. C. Luntz, *J. Phys. Chem. Lett.* **2012**, *3*, 997.
[11] Y.-C. Lu, Z. Xu, H. A. Gasteiger, S. Chen, K. Hamad-Schifferli, Y. Shao-Horn, *J. Am. Chem. Soc.* **2010**, *132*, 12170.
[12] Y.-C. Lu, H. A. Gasteiger, Y. Shao-Horn, *J. Am. Chem. Soc.* **2011**, *133*, 19048.
[13] B. D. McCloskey, R. Scheffler, A. Speidel, D. S. Bethune, R. M. Shelby, A. C. Luntz, *J. Am. Chem. Soc.* **2011**, *133*, 18038.
[14] Z. Peng, S. A. Freunberger, Y. Chen, P. G. Bruce, *Science* **2012**, *337*, 563.
[15] H. D. Lim, H. Song, H. Gwon, K.-Y. Park, J. Kim, Y. Bae, H. Kim, S.-K. Jung, T. Kim, Y. H. Kim, X. Lepro, R. Ovalle-Robles, R. H. Baughman, K. Kang, *Energy Environ. Sci.* **2013**, *6*, 3570.
[16] E. Yilmaz, C. Yogi, K. Yamanaka, T. Ohta, H. R. Byon, *Nano Lett.* **2013**, *13*, 4679.
[17] Z. Jian, P. Liu, F. Li, P. He, X. Guo, M. Chen, H. Zhou, *Angew. Chem., Int. Ed.* **2014**, *53*, 442.
[18] Li, F. ; Y. Chen, D.-M. Tang, Z. Jian, C. Liu, D. Golberg, A. Yamada, H. Zhou, *Energy Environ. Sci.* **2014**, *7*, 1648.
[19] S. Ma, Y. Wu, J. Wang, Y. Zhang, Y. Zhang, X. Yan, Y. Wei, P. Liu, J. Wang, K. Jiang, S. Fan, Y. Xu, Z. Peng, *Nano Lett.* **2015**, *15*, 8084.
[20] D. W. Su, S. X. Dou, G. X. Wang, *J. Mater. Chem. A* **2015**, *3*, 18384.
[21] S. Tong, M. Zheng, Y. Lu, Z. Lin, X. Zhang, P. He, H. Zhou, *Chem. Commun.* **2015**, *51*, 7302.
[22] F. Jiao, P. G. Bruce, *Adv. Mater.* **2007**, *19*, 657.
[23] A. Débart, A. J. Paterson, J. Bao, P. G. Bruce, *Angew. Chem.* **2008**, *120*, 4597.
[24] J. Wu, H. W. Park, A. Yu, D. Higgins, Z. Chen, *J. Phys. Chem. C* **2012**, *116*, 9427.

[25] R. Black, J.-H. Lee, B. Adams, C. A. Mims, L. F. Nazar, *Angew. Chem., Int. Ed.* **2013**, *52*, 392.
[26] W.-H. Ryu, T.-H. Yoon, S. H. Song, S. Jeon, Y.-J. Park, I.-D. Kim, *Nano Lett.* **2013**, *13*, 4190.
[27] G. Zhao, R. Mo, B. Wang, L. Zhang, K. Sun, *Chem. Mater.* **2014**, *26*, 2551.
[28] R. Gao, J. Zhu, X. Xiao, Z. Hu, J. Liu, X. J. Liu, *Phys. Chem. C* **2015**, *119*, 4516.
[29] M. A. Schroeder, A. J. Pearse, A. C. Kozen, X. Chen, K. Gregorczyk, X. Han, A. Cao, L. Hu, S. B. Lee, G. W. Rubloff, M. Noked, *Chem. Mater.* **2015**, *27*, 5305.
[30] S. Ganapathy, Z. Li, M. S. Anastasaki, S. Basak, X.-F. Miao, K. Goubitz, H. W. Zandbergen, F. M. Mulder, M. Wagemaker, *J. Phys. Chem. C* **2016**, *120*, 18421.
[31] K. R. Yoon, G. Y. Lee, G. J.-W. Jung, N.-H. Kim, S. O. Kim, I.-D. Kim, *Nano Lett.* **2016**, *16*, 2076.
[32] P. Zhang, R. Wang, M. He, J. Lang, S. Xu, X. Yan, *Adv. Funct. Mater.* **2016**, *26*, 1354.
[33] P. Zhang, S. Zhang, M. He, J. Lang, A. Ren, S. Xu, X. Yan, *Adv. Sci.* **2017**, *4*, 1700172.
[34] S. H. Oh, L. F. Nazar, *Adv. Energy Mater.* **2012**, *2*, 903.
[35] H. Wang, Y. Yang, Y. Liang, G. Zheng, Y. Li, Y. Cui, H. Dai, *Energy Environ. Sci.* **2012**, *5*, 7931.
[36] F. Li, R. Ohnishi, Y. Yamada, J. Kubota, K. Domen, A. Yamada, H. Zhou, *Chem. Commun.* **2013**, *49*, 1175.
[37] M. M. Ottakam Thotiyl, S. A. Freunberger, Z. Peng, Y. Chen, Z. Liu, P. G. Bruce, *Nat. Mater.* **2013**, *12*, 1050.
[38] J. Xie, X. Yao, I. P. Madden, D.-E. Jiang, L.-Y. Chou, C.-K. Tsung, D. Wang, *J. Am. Chem. Soc.* **2014**, *136*, 8903.
[39] D. Kundu, R. Black; B. Adams; K. Harrison, K. Zavadil, L. F. Nazar, *J. Phys. Chem. Lett.* **2015**, *6*, 2252.
[40] P. Sennu, M. Christy, V. Aravindan, Y.- G. Lee, K. S. Nahm, Y.-S. Lee, *Chem. Mater.* **2015**, *27*, 5726.
[41] F. Li, D.-M. Tang, T. Zhang, K. Liao, P. He, D. Golberg, A. Yamada, H. Zhou, *Adv. Energy Mater.* **2015**, *5*, 1500294.
[42] K. Liao, X. Wang, Y. Sun, D. Tang, M. Han, P. He, X. Jiang, T. Zhang, H. Zhou, *Energy Environ. Sci.* **2015**, *8*, 1992.
[43] D. Kundu, R. Black, E. J. Berg, L. F. Nazar, *Energy Environ. Sci.* **2015**, *8*, 1292.
[44] W. Zhang, Y. Zeng, C. Xu, H. Tan, W. Liu, J. Zhu, N. Xiao, H. H. Hng, J. Ma, H. E. Hoster, R. Yazami, Q. Yan, *RSC Adv.* **2012**, *2*, 8508.
[45] Z. Zhang, G. Zhou, W. Chen, Y. Lai, J. Li, *ECS Electrochem. Lett.* **2013**, *3*, A8.
[46] J. Lu, Y. Qin, P. Du, X. Luo, T. Wu, Y. Ren, J. Wen, D. J. Miller, J. T. Miller, K. Amine, *RSC Adv.* **2013**, *3*, 8276.
[47] F. Wang, X. Wu, C. Shen, Z. Wen, *J. Solid State Electrochem.* **2016**, *20*, 1831.
[48] K. Shimizu, L. Sepunaru, R. G. Compton, *Chem. Sci.* **2016**, *7*, 3364.
[49] M. Sun, Y. Dong, G. Zhang, J. Qu, J. Li, *J. Mater. Chem. A* **2014**, *2*, 13635.
[50] A. Gurlo, N. Bârsan, A. Oprea, M. Sahm, T. Sahm, U. Weimar, *Appl. Phys. Lett.* **2004**, *85*, 2280.
[51] M. V. Reddy, T. Yu, C. H. Sow, Z. X. Shen, C. T. Lim, G. V. Subba Rao, B. V. R. Chowdari, *Adv. Funct. Mater.* **2007**, *17*, 2792.
[52] S. Hao, B. Zhang, S. Ball, J. Wu, M. Srinivasan, Y. Huang, *J. Mater. Chem. A* **2016**, *4*, 16569.
[53] I. Gunasekara, S. Mukerjee, E. J. Plichta, M. A. Hendrickson, K. M. Abraham, *J. Electrochem. Soc.* **2015**, *162*, A1055.
[54] J. Han, X. Guo, Y. Ito, P. Liu, D. Hojo, T. Aida, A. Hirata, T. Fujita, T. Adschiri, H. Zhou, M. Chen, *Adv. Energy Mater.* **2016**, *6*, 1601933.
[55] D. Geng, N. Ding, T. S. A. Hor, S. W. Chien, Z. Liu, D. Wuu, X. Sun, Y. Zong, *Adv. Energy Mater.* **2016**, *6*, 1502164.
[56] B. D. McCloskey, A. Valery, A. C. Luntz, S. R. Gowda, G. M. Wallraff, J. M. Garcia, T. Mori, L. E. Krupp, *J. Phys. Chem. Lett.* **2013**, *4*, 2989.
[57] J. Baltrusaitis, D. M. Cwiertny, V. H. Grassian, *Phys. Chem. Chem. Phys.* **2007**, *9*, 5542.
[58] K. P. C. Yao, D. G. Kwabi, R. A. Quinlan, A. N. Mansour, A. Grimaud, Y.-L. Lee, Y.-C. Lu, Y. Shao-Horn, *J. Electrochem. Soc.* **2013**, *160*, A824.
[59] Z. Li, S. Ganapathy, Y. Xu, J. R. Heringa, Q. Zhu, W. Chen, M. Wagemaker, *Chem. Mater.* **2017**, *29*, 1577.
[60] S. Ganapathy, B. D. Adams, G. Stenou, M. S. Anastasaki, K. Goubitz, X.-F. Miao, L. F. Nazar, M. Wagemaker, *J. Am. Chem. Soc.* **2014**, *136*, 16335.
[61] M. D. Radin, J. F. Rodriguez, F. Tian, D. J. Siegel, *J. Am. Chem. Soc.* **2012**, *134*, 1093.
[62] A. G. Tamirat, J. Rick, A. A. Dubale, W.-N. Su, B.-J. Hwang, *Nanoscale Horiz.* **2016**, *1*, 243.
[63] A. G. B. Williams, M. M. Scherer, *Environ. Sci. Technol.* **2004**, *38*, 4782.
[64] M. Dai, L. Zhao, H. Gao, P. Sun, F. Liu, S. Zhang, K. Shimanoe, N. Yamazoe, G. Lu, *ACS Appl. Mater. Interfaces* **2017**, *9*, 8919.